

Sensitivity of outgoing longwave radiative flux to the global vertical distribution of ozone characterized by instantaneous radiative kernels from Aura-TES

H. M. Worden,¹ K. W. Bowman,² S. S. Kulawik,² and A. M. Aghedo²

Received 22 September 2010; revised 26 April 2011; accepted 4 May 2011; published 28 July 2011.

[1] We calculate the sensitivity of outgoing longwave radiation (OLR) to the global vertical distribution of tropospheric ozone using ozone profile estimates from Aura Tropospheric Emission Spectrometer (Aura-TES) along with the partial derivatives of spectral radiance with respect to ozone from the Aura-TES operational retrieval algorithm. Accounting for anisotropy, we calculate top of atmosphere instantaneous radiative kernels (IRKs), in $\text{W/m}^2/\text{ppb}$, for infrared ozone absorption from 985 to 1080 cm^{-1} . Zonal mean distributions for August 2006 show significant variations in the IRK between clear and cloudy sky, ocean and land, and day and night over land. For all sky (clear and cloudy conditions), OLR is significantly less sensitive to ozone in the middle and lower troposphere due to clouds, especially in the tropics. We also compute the longwave radiative effect (LWRE), i.e., the reduction in OLR due to absorption by tropospheric ozone, and find a global average LWRE of $0.33 \pm 0.02^{+0.018}_{-0.007}\text{ W/m}^2$ (with uncertainty and bias) for tropospheric ozone with significant variability ($\sigma = 0.23\text{ W/m}^2$) under all sky conditions for August 2006. For clear sky, tropical conditions we examine the effect of water vapor in reducing the LWRE from tropospheric ozone.

Citation: Worden, H. M., K. W. Bowman, S. S. Kulawik, and A. M. Aghedo (2011), Sensitivity of outgoing longwave radiative flux to the global vertical distribution of ozone characterized by instantaneous radiative kernels from Aura-TES, *J. Geophys. Res.*, 116, D14115, doi:10.1029/2010JD015101.

1. Introduction

[2] Tropospheric ozone plays a critical role in climate, atmospheric chemistry and air pollution. Due to significant increases in anthropogenic emissions since preindustrial times, tropospheric ozone has the third highest impact as a greenhouse gas in terms of direct radiative forcing (IPCC Fourth Assessment Report (AR4)) [Solomon *et al.*, 2007], but is distinguished from other greenhouse gases by having significant spatial and temporal heterogeneity due to the relatively short lifetime, approximately 22 days in the troposphere [Stevenson *et al.*, 2006], and large global variations of ozone precursors. The radiative forcing from tropospheric ozone (with respect to the tropopause) estimated in the IPCC TAR (Third Assessment Report) [Ramaswamy *et al.*, 2001] was $+0.35 \pm 0.15\text{ W/m}^2$ and did not change significantly in the IPCC AR4. This radiative forcing corresponds to a global mean increase of 9 DU (Dobson Units) in tropospheric ozone from pre-industrial amounts. Ozone is an essential part of the oxidative capacity of the atmosphere as the precursor of the hydroxyl radical, OH.

Ozone chemical loss is dominated by reactions with water vapor, after photolysis, and HO_x ($\text{HO}_2 + \text{OH}$). Ozone destruction in turn decreases methane lifetime, which is the second most important greenhouse gas. These interactions lead to chemistry-climate feedbacks with water vapor and methane [Stevenson *et al.*, 2006]. In addition, ozone has climate impacts through the carbon and hydrological cycles by reducing global primary productivity and therefore the CO_2 uptake by biota (plants, forests). For example, Sitch *et al.* [2007] estimated that suppression of CO_2 uptake due to ozone damage could lead to an indirect radiative forcing of 0.62 to 1.09 W/m^2 .

[3] Studies since the IPCC AR4 have found that changes in short-lived species, including tropospheric ozone, are expected to have a significant impact on global temperatures, especially over the northern hemisphere [Levy *et al.*, 2008a]. In particular, by 2050, short-lived air pollutants could be responsible for up to 20% of simulated global mean annually averaged warming and up to 40 percent of the total projected summertime warming in the central United States from 2050 to 2100 [Levy *et al.*, 2008b]. However, the contribution of short-lived species to simulated change in global mean surface temperature can have a strong dependence on its spatial variability [Shindell and Faluvegi, 2009]. All of these factors have led to an increasing interest in policies that mitigate both air quality and global warming [West *et al.*, 2006, 2007; van Vuuren *et al.*, 2006; Wallack and Ramanathan, 2009; Ramanathan and

¹Atmospheric Chemistry Division, National Center for Atmospheric Research, Boulder, Colorado, USA.

²Jet Propulsion Laboratory, California Institute of Technology, Pasadena, California, USA.

Xu, 2010], with the concomitant need for accurate measurements and model results.

[4] As discussed in several studies [e.g., *Lacis et al.*, 1990; *Forster and Shine*, 1997; *Gauss et al.*, 2003], radiative forcing of ozone depends strongly on the vertical distribution of ozone abundance, with both positive (longwave) and negative (shortwave) forcings for increases in lower stratospheric ozone, and only positive (both longwave and shortwave) forcings for increases in tropospheric ozone. Within the troposphere, there is also a strong vertical dependence of ozone forcing due to thermal contrast, humidity, clouds and variability of ozone itself. In this paper, we compute the longwave radiative effect (LWRE) due to ozone with respect to the TOA (top of atmosphere) radiative flux as observed from space by the Aura-TES (Tropospheric Emission Spectrometer). This is distinguished from radiative forcing as defined by the IPCC [*Ramaswamy et al.*, 2001], which is the difference in total irradiance (flux) at the tropopause due to the changes from pre-industrial to present concentrations. Although the tropopause has been a useful reference point in these climate simulations, we note that the TOA radiative flux is a critical component of the planetary radiative balance that can be directly measured by satellites and is therefore useful in ensemble climate model evaluation. Since the OLR is insensitive to changes in tropopause height, which are also expected with climate change [e.g., *Santer et al.*, 2003; *Seidel and Randel*, 2007], the TOA provides a complimentary reference point for investigating radiative forcing and feedbacks [*Soden et al.*, 2008].

[5] In conjunction with satellite measurements, we utilize the concept of the “radiative kernel” (RK) which was introduced by *Soden et al.* [2008] to quantify radiative feedbacks in climate models. The RK discussed by *Soden et al.* represents the derivative of the TOA radiative flux with respect to a change in an atmospheric variable at each altitude averaged over some spatiotemporal domain whereas the “instantaneous” radiative kernel (IRK) presented here is sensitivity of the TOA radiative flux to each observed ozone profile.

[6] There have only been a few previous studies using satellite data to quantify the longwave radiative effects of ozone [*Harries et al.*, 2001; *Worden et al.*, 2008; *Joiner et al.*, 2009]. *Worden et al.* [2008] used linear regressions between upper tropospheric subcolumns from TES ozone profiles and corresponding outgoing spectral radiance to approximate IRKs. However, these empirical calculations were only possible for cloud free, ocean scenes. In this study, we apply the analytic Jacobians of spectral radiance calculated from the TES operational retrieval algorithm to perform a more accurate, radiatively consistent IRK calculation that accounts explicitly for all the contributions to flux variability in the 9.6 μm ozone band, including clouds, surface temperature and emissivity, atmospheric temperature, water vapor and ozone itself. These IRKs have been used to investigate the equivalent radiative effects of differences between climate model and observed ozone distributions from *Aghedo et al.* [2011].

[7] This paper is organized as follows. Section 2 describes Tropospheric Emission Spectrometer (TES) measurements and their validation. Section 3 presents the methods for computing IRKs. Section 4 is a discussion of the IRK spatial distributions. Section 5 describes the LWRE from tropo-

spheric ozone and compares this to previous results. Section 6 summarizes the results and gives plans for future work.

2. Tropospheric Emission Spectrometer

[8] Launched in July 2004 on the NASA EOS-Aura platform, the Tropospheric Emission Spectrometer (TES) is an infrared (IR) Fourier Transform Spectrometer (FTS). Aura is in a near-polar, Sun-synchronous orbit with equator crossing times of 13:40 and 2:29 local mean solar time for ascending and descending orbit paths, respectively. TES measures radiance spectra of the Earth’s surface and atmosphere at frequencies between 650–2250 cm^{-1} with unapodized spectral resolution of 0.06 cm^{-1} [*Beer*, 2006]. This spectral resolution is sufficient to resolve pressure-broadened IR absorption lines in the troposphere and allows TES to estimate simultaneous, collocated vertical profiles of IR-active trace gases including ozone, water vapor, carbon monoxide, methane, deuterated water vapor as well as atmospheric temperature. Effective cloud pressure and optical depth, surface temperature and land emissivity are also derived from TES radiance spectra. Algorithms for radiometric calibration [*Worden et al.*, 2006], retrieval of atmospheric parameters [*Bowman et al.*, 2006], and error characterization [*Worden et al.*, 2004] along with cloud property retrievals [*Kulawik et al.*, 2006] have been described previously. The TES forward model used for computing spectral radiances and Jacobians [*Clough et al.*, 2006] is based on LBLRTM (line-by-line radiative transfer model), which has been used to calculate atmospheric heating and cooling rates [*Clough and Iacono*, 1995].

[9] TES radiances have been compared to collocated spectral radiances from Aqua-AIRS (Atmospheric Infrared Sounder), which is ~ 15 min ahead of Aura along the same orbital path and from underflights of the Scanning High-Resolution Interferometer Sounder (S-HIS) on the NASA WB57 [*Shephard et al.*, 2008]. For the integrated 9.6 μm ozone band, TES radiances have 0.12K cold bias with respect to AIRS, which is within the expected accuracy (0.2K) for AIRS radiance measurements [*Tobin et al.*, 2006]. TES cloud retrievals have been validated using the Aqua Moderate Resolution Imaging Spectroradiometer (MODIS) and AIRS [*Eldering et al.*, 2008].

[10] From the context of OLR, TES is sensitive to patterns of ozone variation that have an impact on outgoing longwave radiation and is insensitive to patterns of variation that do not have a strong impact on spectrally resolved OLR variability. Consequently, while tropospheric ozone can be highly variable, only about 1–2 degrees of freedom [*Worden et al.*, 2004] in that variability have a measurable effect on outgoing OLR. However, this information is spread throughout the vertical pressure grid, which is necessary to accurately calculate TOA spectral radiances. TES retrievals are reported on a 66-level pressure grid (given in Appendix B). Although the ozone parameters on these vertical levels are not independent, the errors and correlation are characterized by the TES retrieval system and reported for each retrieval [*Bowman et al.*, 2006].

[11] TES ozone profiles have a consistent high bias, $\sim 15\%$ (~ 10 ppb) in the troposphere, relative to ozonesondes [*Nassar et al.*, 2008] and aircraft data [*Richards et al.*, 2008]. TES ozone columns (total, stratospheric and tropospheric) have been validated using ozonesondes and other satellite mea-

measurements from OMI (Ozone Monitoring Instrument) and MLS (Microwave Limb Sounder) on Aura [Osterman *et al.*, 2008], also showing a consistent high bias for the TES measurements. Some of the high bias can be expected from known discrepancies for ozone absorption (5.5%) between IR and UV spectroscopic line parameters that are persistent in the HITRAN database since HITRAN2003 [Picquet-Varrault *et al.*, 2004]. High biases for ozone retrieved from IR remote sensing compared to UV have been observed consistently in ground-based FTIR [Schneider *et al.*, 2008] and IR satellite instruments [e.g., Boynard *et al.*, 2009; Osterman *et al.*, 2008; Nassar *et al.*, 2008].

3. Instantaneous Radiative Kernel Formulation

[12] The instantaneous radiative kernel (IRK) is defined as the sensitivity of the TOA radiative flux to changes in the vertical distribution of an atmospheric parameter given by:

$$\frac{\partial F_{TOA}}{\partial q(z_l)} = \int_{\nu} \int_0^{2\pi} \int_0^{\frac{\pi}{2}} \frac{\partial L_{TOA}(\nu, \theta, \phi)}{\partial q(z_l)} \cos \theta \sin \theta d\theta d\phi d\nu, \quad (1)$$

where F_{TOA} is the TOA flux, q is the atmospheric parameter (e.g., ozone abundance at a vertical level z_l), L_{TOA} is the upwelling TOA radiance at zenith angle θ , azimuth angle ϕ , and frequency ν . Since we only have nadir measurements ($\theta = 0$), we use an estimate of anisotropy, R , (described below), to account for the angular integration with directional dependence. We then have:

$$\frac{\partial F_{TOA}}{\partial q(z_l)} = \int_{\nu} \frac{\partial L_{TOA}(\nu, \theta = 0)}{\partial q(z_l)} \frac{\pi d\nu}{R(\nu, \theta = 0)}. \quad (2)$$

The partial derivatives of radiance L with respect to q for each frequency, i.e., weighting functions or Jacobians, are provided by the TES operational radiative transfer algorithm, [Clough *et al.*, 2006], and are used within the retrieval algorithm to estimate the vertical distributions of trace gases [Bowman *et al.*, 2006]. Using the Jacobians from the last retrieval iteration, the IRK is computed through the following steps: (1) conversion of the atmospheric state from the logarithm of the volume mixing ratio (VMR), used for retrieval parameters, to either VMR in ppb (parts per billion) or partial column in Dobson Units; (2) applying spectral anisotropy estimate to calculate a spectrally dependent flux sensitivity in $W/cm^2/cm^{-1}/ppb$ or $W/cm^2/cm^{-1}/DU$; and (3) spectral integration over thermally sensitive regions to obtain IRKS, i.e., derivatives of TOA flux with respect to the vertical distribution of a trace gas in $(W/m^2)/ppb$ or $W/cm^2/DU$. These steps are detailed in sections 3.1–3.3 along with error estimation in section 3.4.

3.1. TES Radiance Jacobians

[13] The Jacobians calculated during the operational TES retrieval represent the sensitivity of the TOA spectral radiances (in $W/cm^2/sr/cm^{-1}$) of given viewing angle to the atmospheric state at each vertical level. In the case of trace gases, the atmospheric state is represented in the natural log of volume mixing ratio, i.e., $\ln(\text{VMR})$, with corresponding Jacobian units $W/cm^2/sr/cm^{-1}/\ln(\text{VMR})$. Jacobians are computed for each atmospheric layer and mapped to pressure levels, given in

Appendix B. Since TES retrievals are performed for all scene types: land, ocean, cloudy and cloud-free, the stored Jacobians are a unique data set for studying a wide range of actual TOA radiance conditions and their responses to changes in the vertical distribution of ozone. Here we use TES V3 retrievals as the starting point for computing forward model spectra and Jacobians for the full IR ozone band from 985 to 1080 cm^{-1} . Only good quality retrievals were selected by applying the master quality flag (removes $\sim 18\%$ of retrievals) along with additional screening for emission layer and c-curve cases ($\sim 5\%$ of retrievals) to remove nonconvergent and unphysical ozone profiles [Osterman *et al.*, 2009]. The rejected profiles are not biased with respect to spatial or cloud parameters, except for scenes with known retrieval problems in Antarctica.

[14] As the first step in computing IRKS, we convert the stored Jacobians as follows:

$$\frac{\partial L_{TOA}}{\partial q(z_l)} = \frac{1}{q(z_l)} \frac{\partial L_{TOA}}{\partial \ln q(z_l)}, \quad (3)$$

where L_{TOA} is the TOA radiance, q is the VMR in ppb at vertical layer z_l . This results in Jacobians with units of $W/cm^2/sr/cm^{-1}/ppb$. The Jacobians may also be calculated with respect to ozone subcolumns in Dobson Units (DU):

$$\frac{\partial L_{TOA}}{\partial col} = \frac{\partial L_{TOA}}{\partial q(z_l)} \frac{\partial q(z_l)}{\partial col} = \frac{\partial L_{TOA}}{\partial q(z_l)} \left(\frac{2.687 \cdot 10^{16}}{\rho_l \Delta z_l} \right), \quad (4)$$

where col is the layer column in DU, ρ_l is layer density (in molecules/ cm^3), Δz_l is the layer height in cm and 1 DU = $2.687 \cdot 10^{16}$ molecules/ cm^2 . Since we are dividing by the retrieved ozone abundance to obtain our sensitivity as a function of VMR or column, we must correct for the observed bias in TES retrieved ozone values. The validation results show that TES ozone in the troposphere is too high by $15\% \pm 5\%$ [Nassar *et al.*, 2008], which is due to instrument or retrieval accuracy as well as the known problems with IR ozone line parameters described above.

[15] Figure 1 shows TES radiance Jacobians for ozone and water vapor for a single observation with respect to VMR and $\ln(\text{VMR})$. The units in which the sensitivity is expressed have a significant impact on the vertical distribution of that sensitivity. In terms of $\ln(\text{VMR})$, the greatest sensitivity to ozone is in the stratosphere. Changes in $\ln(\text{VMR})$ can be approximated by fractional changes in the state and relative increases in ozone in the stratosphere, where the concentration is highest, will have the largest impact on TOA radiance. Conversely, sensitivity to changes in absolute ozone is highest in the midtroposphere from around 500 to 700 hPa. Consequently, retrievals of ozone from spectrally resolved thermal IR instruments have their greatest sensitivity in the midtroposphere [e.g., Bowman *et al.*, 2002, Boynard *et al.*, 2009]. We have included the Jacobians for water vapor in Figure 1 to demonstrate how TES spectral resolution allows us to compute ozone sensitivity in the presence of water vapor. Note that ozone absorption lines that are obscured by strong water vapor lines or continuum will have little impact on the frequency-integrated Jacobians. Figure 1 shows the Jacobians in terms of negative radiance per solid angle per wave number per abundance, since the TOA radiance is reduced with increasing abundance of gases in absorption. For the IRK

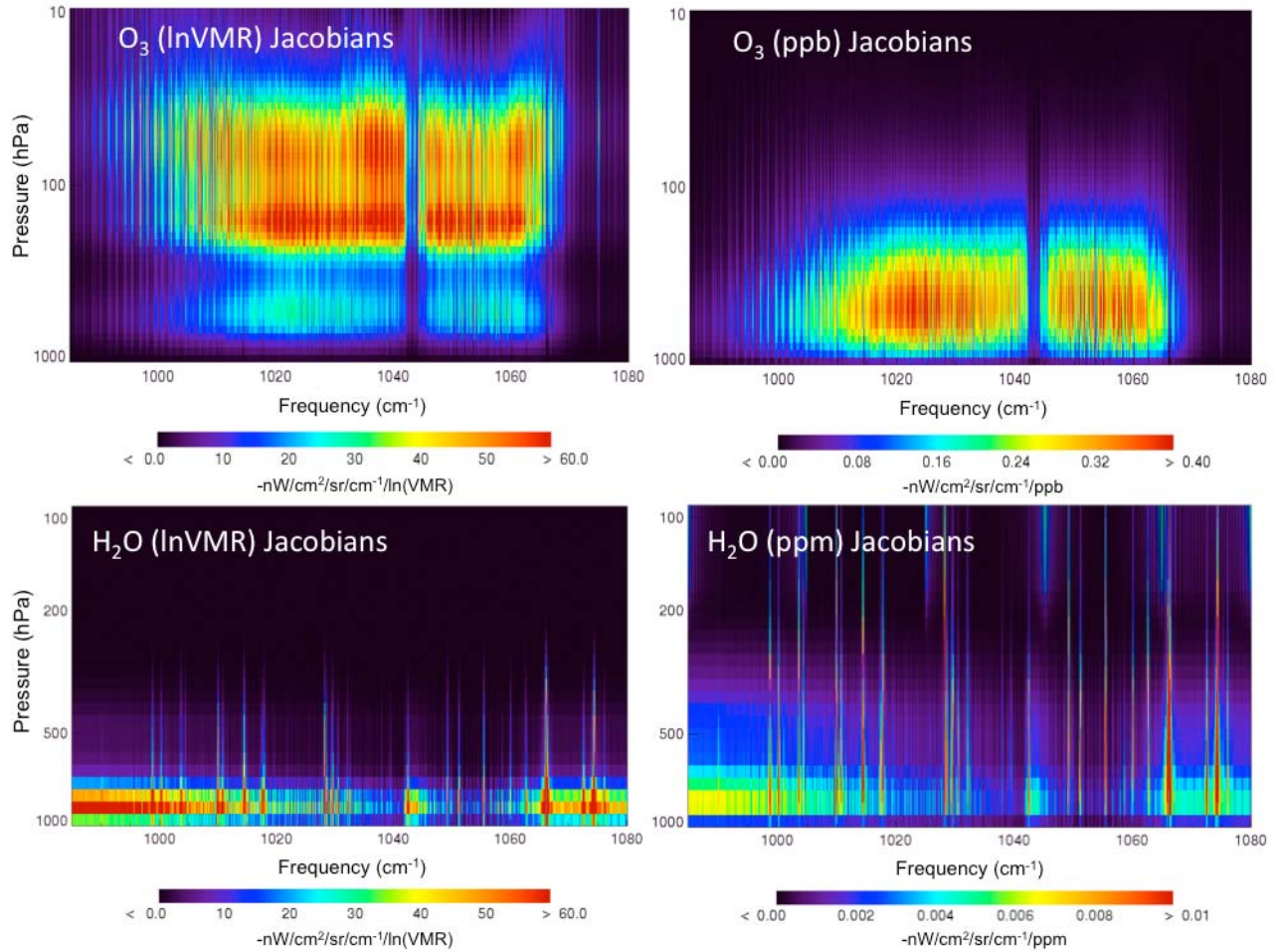


Figure 1. TES ozone and water vapor Jacobians in the $9.6 \mu\text{m}$ ozone band for a single TES nadir observation at 65°N , taken in August 2006, with surface temperature = 295 K. (left) The Jacobians with respect to $\ln(\text{VMR})$. (right) The Jacobians with respect to ppb for O_3 and ppm for H_2O . Note the different pressure range for (top) O_3 compared to (bottom) H_2O .

formulation, we follow the convention that a reduction in TOA flux corresponds to a positive forcing and therefore we present results as positive quantities.

3.2. Anisotropy Estimate

[16] In order to perform the angular integration in equation (1), we use an estimate of anisotropy, $R(\theta)$, (where $\theta = 0$, for TES nadir views), for each frequency ν , defined as:

$$R_\nu(\theta) = \pi L_\nu(\theta) / F_\nu. \quad (5)$$

For broadband radiometers such as the Earth Radiation Budget Experiment (ERBE) and the Clouds and Earth's Radiant Energy System (CERES) [Loeb *et al.*, 2003] estimates of anisotropy, also called angular distribution models (ADMs), vary significantly with cloud coverage and emissivity, day, night, land surface type, temperature lapse rate and precipitable water vapor. Because of this variability, as well as the TES spectral dependence, we need an efficient method of estimating anisotropy for each TES observation.

[17] We found that a single angle approximation to the flux gave sufficient accuracy, quantified below, as compared to 3-point and 5-point Gaussian Quadrature (GQ) results

[e.g., Li, 2000] and also agreed with the magnitude and spectral behavior of anisotropy estimates used to compute fluxes from AIRS radiances by Huang *et al.* [2008, 2010]. This allows estimates of anisotropy that only require one extra radiance calculation per TES observation, however, improved accuracy could be obtained by using 3-point GQ, as shown in Appendix A.

[18] If we assume azimuthal symmetry, for target zenith angles θ , we can write:

$$R_\nu(\theta = 0) = \frac{\pi L_\nu(0)}{\int_0^{2\pi} \int_0^{\frac{\pi}{2}} L_\nu(\theta) \cos \theta \sin \theta d\theta d\phi} = \frac{L_\nu(0)}{2 \int_0^{\frac{\pi}{2}} L_\nu(\theta) \cos \theta \sin \theta d\theta} \quad (6)$$

and if we let $x = \cos \theta$, then $dx = -\sin \theta d\theta$ so that:

$$\int_0^{\frac{\pi}{2}} L_\nu(\theta) \cos \theta \sin \theta d\theta = \int_0^1 L(\cos^{-1} x) x dx = \int_0^1 x^k f(x) dx \approx \sum_{i=1}^n w_i f(x_i). \quad (7)$$

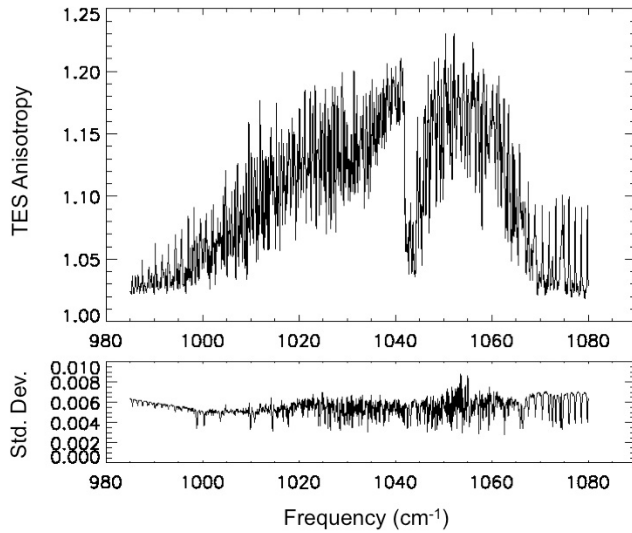


Figure 2. Estimated spectral anisotropy for the 9.6 μm ozone band for clear sky ocean conditions. The (top) average and (bottom) standard deviation for 31 clear-sky Atlantic Ocean scenes, 16°N–30°N, taken 11 August 2006.

Using tabulated abscissas x_i and weight factors w_i in “Abcissas and Weight Factors for Gaussian Integration of Moments,” Table 25.8 [Abramowitz and Stegun, 1972] we have for $n = 1$, $k = 1$:

$$x_i = 0.666667 \text{ and } w_i = 0.50$$

for $x = 0.666667$, $\theta = \cos^{-1}(0.666667) = 48^\circ$. We then have:

$$R_\nu(\theta = 0) = \frac{L_\nu(0)}{2[0.5L_\nu(48^\circ)]} = \frac{L_\nu(0)}{L_\nu(48^\circ)}. \quad (8)$$

Figure 2 shows the spectral anisotropy estimate for a clear sky ocean case. A comparison of this estimate to anisotropy calculations from 3-point and 5-point GQ as well as the standard diffusivity angle ($\theta = 53^\circ$) approximation for single target scenes (clear and cloudy cases) is shown in Appendix A. We find that the diffusivity angle approximation is not as accurate as our 1-point GQ estimate in the 9.6 μm ozone band. The 1-point GQ estimate has a systematic bias of 2% when integrated over the ozone band compared to 5-point GQ in the clear-sky ocean case we tested, with a smaller bias (1.5%) for the cloud case. Appendix A also shows comparisons of TES anisotropy estimates, extrapolated for the 8–12 μm window region, to tabulated CERES values for clear sky nadir cases, showing that TES values have the same dependence of ocean to land, day to night and increase with precipitable water vapor as CERES.

3.3. Radiative Kernel and Application to Differences in Ozone Distributions

[19] From equation (2), we replace the integral over frequency with a sum over the ozone band frequencies for TES sampling $\Delta\nu$ and converting area to m^2 , we compute the ozone IRK as:

$$\frac{\partial F_{\text{TOA}}}{\partial q(z_l)} = \frac{1}{q(z_l)} \sum_\nu \frac{\pi \Delta\nu}{R(\nu)} \frac{\partial L_{\text{TOA}}(\nu)}{\partial \ln q(z_l)} 10^4 (\text{cm}^2/\text{m}^2) \quad (9)$$

in $\text{W}/\text{m}^2/\text{ppb}$ for vertical layer z_l . We can also define a logarithmic instantaneous radiative kernel (LIRK) with respect to $\ln(\text{VMR})$ Jacobians:

$$\frac{\partial F_{\text{TOA}}}{\partial \ln q(z_l)} = \sum_\nu \frac{\pi \Delta\nu}{R(\nu)} \frac{\partial L_{\text{TOA}}(\nu)}{\partial \ln q(z_l)} 10^4 (\text{cm}^2/\text{m}^2). \quad (10)$$

If we use the $\ln(\text{VMR})$ Jacobians directly, we have a radiative kernel in units of W/m^2 for each vertical layer z_l that represents the change in TOA radiance due to the fractional ozone abundance at each level. This quantity is equivalent to the longwave radiative effect (LWRE) discussed in section 5 and can also be used to compute the change in TOA radiative flux corresponding to a fractional perturbation in an O_3 profile, described below.

[20] Although it is possible to create radiative kernels for other species, e.g., water vapor, carbon dioxide or methane using this method, we restrict our attention to ozone in the 9.6 μm band which covers almost all of the longwave ozone absorption, with other IR ozone bands contributing less than $\sim 3\%$ due to weaker line strengths, lower thermal radiance and atmospheric opacity from strong CO_2 or H_2O absorption [e.g., Rothman *et al.*, 1987]. Therefore, the radiative kernels given in equations (9) and (10) give an accurate representation of the differential response in TOA longwave flux due to a change in the vertical distribution of ozone. The application of this technique to other molecules that impact a broader frequency range of thermal radiances, e.g., water vapor, is the subject of future research.

[21] For a given location and sample time i , we can define an operator $\mathbf{H}_i(z_l)$ equal to the ozone IRK in equation (9) at those coordinates for the average altitude z corresponding to layer l . This operator can be used to assess the TOA longwave radiative effect, Δ_{LWRE} , in W/m^2 , due to a difference in ozone abundance, e.g., the difference of model (sim) to observation or some other reference (ref):

$$\Delta_{\text{LWRE}} = \mathbf{H}_i(z_l) [q_i^{\text{sim}}(z_l) - q_i^{\text{ref}}(z_l)] = \frac{\partial F_{\text{TOA}}^i}{\partial q_i(z_l)} [q_i^{\text{sim}}(z_l) - q_i^{\text{ref}}(z_l)] \quad (11)$$

or for fractional changes

$$\Delta_{\text{LWRE}} = \mathbf{H}_i^{\ln}(z_l) \left[\ln \frac{q_i^{\text{sim}}(z_l)}{q_i^{\text{ref}}(z_l)} \right] = \frac{\partial F_{\text{TOA}}^i}{\partial \ln q_i(z_l)} \left[\ln \frac{q_i^{\text{sim}}(z_l)}{q_i^{\text{ref}}(z_l)} \right]. \quad (12)$$

The TES radiative kernel operator in equation (11) was applied by Aghedo *et al.* [2011] to examine the TOA radiative effect associated with model-to-observation differences for tropospheric ozone calculated by four different global chemistry climate models. (We note that Aghedo *et al.* [2011] used the terminology of Instantaneous Radiative Forcing Kernels, IRFKs, while we use IRKs here. These should be considered equivalent). Aghedo *et al.* [2011] found aggregate LWRE biases in the troposphere that range from -0.4 to $+0.7 \text{ W}/\text{m}^2$ over large regions in the tropics and the midlatitudes. The biases are due to ozone differences between model and observations throughout the troposphere, especially in the lower and middle troposphere over the tropics and the midlatitudes.

Table 1. Error Budget for TES Instantaneous Radiative Kernels (IRK)

Error Source	Random	Systematic
A posteriori retrieval error	±20%	
O ₃ retrieval bias	±5% (uncertainty in retrieval bias)	−15% IRK increased by 15%
Anisotropy	±3.3% (all sky)	+2% (IRK too high)
Total error	±22%	+2%

3.4. Error Estimation

[22] Uncertainties in the TES radiative kernel are due to the ozone retrieval, the correction for ozone retrieval bias and the anisotropy estimate. We note that further work is required to assess bias and uncertainties due to TES sampling, for both clear and cloudy conditions, so here we present the error budget in the case of a single TES IRK estimate. The ozone retrieval error, around 20% in the troposphere, includes radiance errors and cross-state errors due to the simultaneous retrieval of temperature, but is dominated by smoothing error as discussed by *Bowman et al.* [2006]. As stated above, we incur a 5% uncertainty from the ozone bias correction. The anisotropy estimate is biased low, giving a 2% high bias in the IRK. Random errors in anisotropy are approximated by the observed variability, ~1.8% for clear sky and 3.3% for all sky. From Appendix A, average differences of TES-CERES anisotropy for clear sky cases, ranging from 0.5% to 1.6% (ocean to land) are consistent with this approximation. Table 1 provides a summary of these error terms. Assuming these errors are uncorrelated, the total random error is ±22% for TES IRKs, with a bias error of +2%.

[23] For the LIRK in equation (10), (or LWRE), we do not divide by the retrieved ozone with associated smoothing errors and retrieval bias. We can then estimate the measurement error using the spectral fit from the retrieval, i.e., the RMS residual of forward model minus the measured radiance, which will include both measurement noise and forward model errors. This error indicates how well the Jacobians performed to match the model and measured radiances at retrieval convergence, within the noise. For good quality TES retrievals, the RMS residual is around 30 nW/cm²/sr/cm^{−1} in the O₃ band, corresponding to 0.08 W/m² for the TOA flux. Summing the total LWRE (including the stratosphere) over the ozone band gives 2.1 W/m² average for clear sky and 1.6 W/m² average for all sky. Adding the fractional error from the residual in quadrature to the anisotropy error given above yields uncertainties of ±4.3% for clear sky and ±6% for all sky in our tropospheric ozone LWRE estimates. We account for systematic errors in the LWRE estimates with asymmetric error terms for the low bias in Jacobians due to ozone IR line parameters (+5.5%) and the high bias from anisotropy (−2%). We note that we are assuming the line parameter error applies to the entire integrated spectral range, which is likely an overestimate for this bias. The random and systematic errors for LWRE (also LIRK) are given in Table 2.

4. IRK Distributions

[24] To examine the behavior of TES-derived IRKs for different observation scenes, we computed spectral Jaco-

biens and anisotropy for all the August 2006 TES retrievals. This yielded 41510 samples for all sky conditions where the retrievals passed the quality tests suggested for TES V003 data [*Osterman, 2009*]. Of these, 13509 cases were considered to be clear sky using the criteria of retrieved effective cloud optical depth <0.1. Further classification to ocean or land surface type is done using the surface flag determined from the digital elevation model (DEM) used by the TES L1 algorithms [*Worden et al., 2006*].

[25] Figure 3 shows zonal averages of ozone IRKs expressed with respect to changes in ozone mixing ratio (ppb) for clear and all sky conditions, each separated into ocean, land/night and land/day surface types. Latitudinal discontinuities in the land IRKs are due to varying land types (especially for Austral winter) and relatively small samples (N~10 to 50) in the southern hemisphere. We see maximum sensitivity in the middle troposphere (centered around 450 hPa, between 300 and 600 hPa) for clear sky conditions. For all of the surface types, the maximum sensitivity to ozone is shifted upwards (toward the tropopause) for cloudy scenes. Similar behavior is noted for the radiative kernels modeled by *Soden et al.* [2008] for atmospheric temperature and water vapor where clouds significantly reduce the sensitivity to parameters in the lower troposphere compared to the clear sky kernels.

[26] Figure 4 shows the same cases as Figure 3, but for ozone IRKs expressed with respect to column changes in ozone (DU). These IRKs have a very different vertical dependence, with maximum sensitivity close to the tropopause. The sensitivity in Figure 3 (W/m²/ppb) is shifted to the middle troposphere since a unit change in ozone abundance produces a larger change in the ozone column lower in the atmosphere. This is the reason IR spectrometers have peak sensitivity to trace gas abundance profiles in the midtroposphere compared to the upper troposphere, which has more thermal contrast with the surface. We report the IRKs on the TES pressure grid listed in Appendix B since these values are self-consistent with the measured TOA radiance, but we note that there is an implicit dependence on the pressure grid that could be removed by a normalization using the pressure grid spacing to give results in W/m²/ppb/hPa. This pressure normalization (not shown) has a similar effect to converting from VMR to subcolumns in shifting the maximum sensitivity toward the tropopause since the pressure grid spacing (see Appendix B) is reduced at lower pressure.

[27] The vertical sensitivity with respect to column ozone shown in Figure 4 is consistent with previous studies examining changes in column ozone [e.g., *Lacis et al., 1990*] that showed the forcing peaks near the tropopause. However, as noted in the introduction, these IRKs give the

Table 2. Error Budget for TES Ozone Longwave Radiative Effect (LWRE) or Logarithmic Instantaneous Radiative Kernels

Error Source	Random		Systematic
	Clear Sky	All Sky	
Radiance Residual	±3.8%	±5.0%	
Anisotropy	±1.8%	±3.3%	+2% (LWRE too high)
Spectroscopy			−5.5%
Total error	±4.3%	±6.0%	+2%, −5.5%

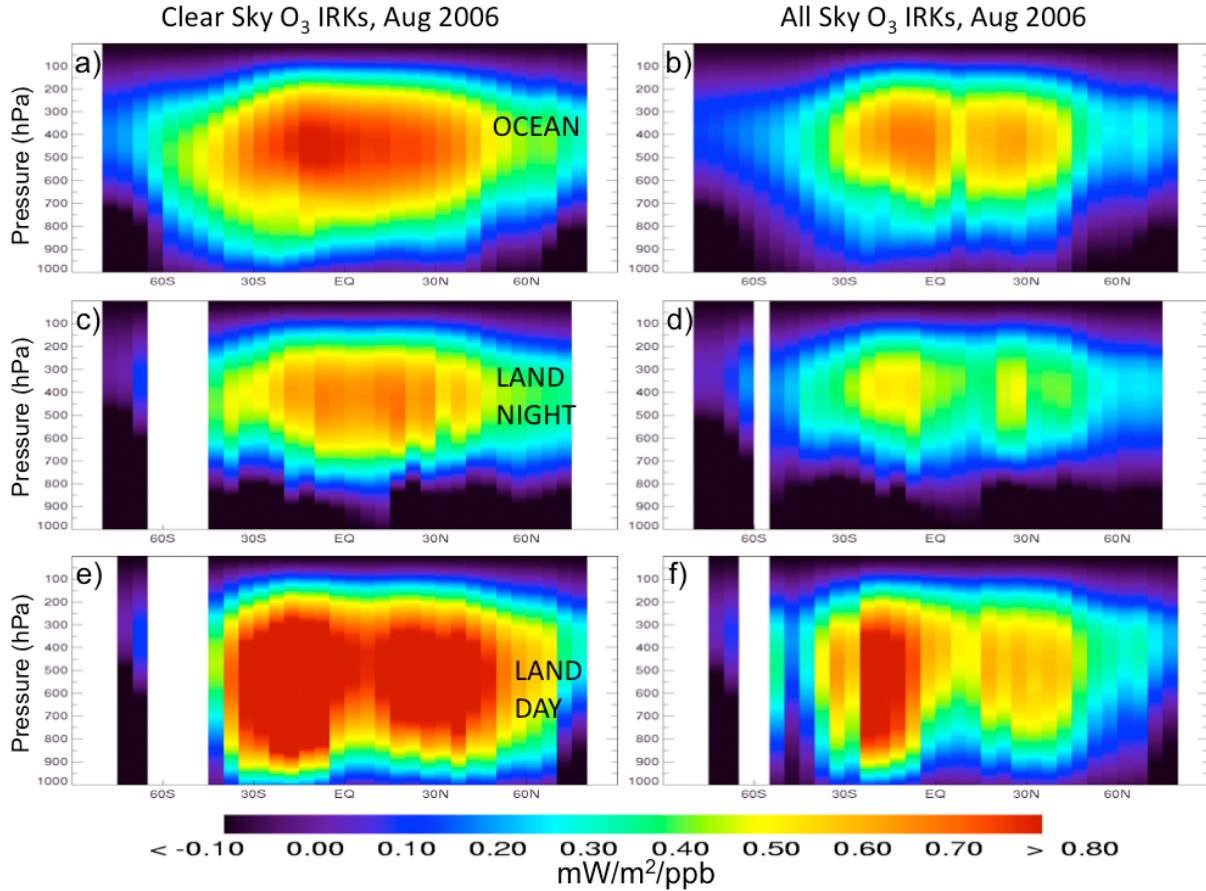


Figure 3. Zonal average IRKs in $\text{mW/m}^2/\text{ppb}$ for (a) clear-sky ocean ($N_{\text{avg}} = 294$), (b) all sky ocean ($N_{\text{avg}} = 870$), (c) clear-sky land, night, ($N_{\text{avg}} = 52$), (d) all sky land, night, ($N_{\text{avg}} = 165$), (e) clear-sky land, day ($N_{\text{avg}} = 76$), and (f) all-sky land, day ($N_{\text{avg}} = 228$). N_{avg} is the average number of TES samples per 5° latitude bin in each type of scene.

sensitivity of the TOA longwave flux to ozone and do not represent the dependence of anthropogenic radiative forcing on ozone. Figure 5 summarizes the vertical dependence of the clear versus all sky average IRKs with respect to ozone changes in both mixing ratio and column.

5. Longwave Radiative Effect Distributions

[28] We define the longwave radiative effect (LWRE) for tropospheric ozone as the reduction in OLR due to tropospheric ozone with respect to each observed atmospheric state. Assuming linearity in the change to OLR, the LWRE can be derived from equation (11) by using the retrieved profile and assuming a reference of zero, which cancels the retrieved profile in the denominator of equation (9). This is equivalent to the LIRK in equation (10) or an application of the operator in equation (12) to unity. Since we evaluate the LIRK or LWRE at each vertical level in equation (10), we can obtain estimates of the LWRE for tropospheric sub-columns by summing over the appropriate vertical levels in equation (10), with the corresponding error budget given in Table 2.

[29] The reduction in OLR due to upper tropospheric ozone was also computed empirically using TES ozone retrievals and radiance spectra for 2006, 45°S to 45°N from Worden *et al.* [2008], with an annual average LWRE of $0.48 \pm 0.14 \text{ W/m}^2$ and significant variability (standard deviation = 0.24 W/m^2). These previous calculations were only possible for clear sky ocean observations and the upper tropospheric column was computed for 500 hPa to 200 hPa to provide a consistent column definition over the latitude range.

[30] The new approach used here improves the accuracy of the ozone LWRE estimate in 3 ways:

[31] 1. The previous estimate used slopes from linear regressions of the ozone band flux variation with upper tropospheric ozone columns as a function of SST (sea surface temperature). This previous approach could not completely remove the effects of water vapor and the OLR sensitivity to ozone was likely overestimated. In this new approach, water vapor interference is explicitly removed by summing over the fine spectral resolution ozone Jacobians, which only include the sensitivity to ozone, by definition.

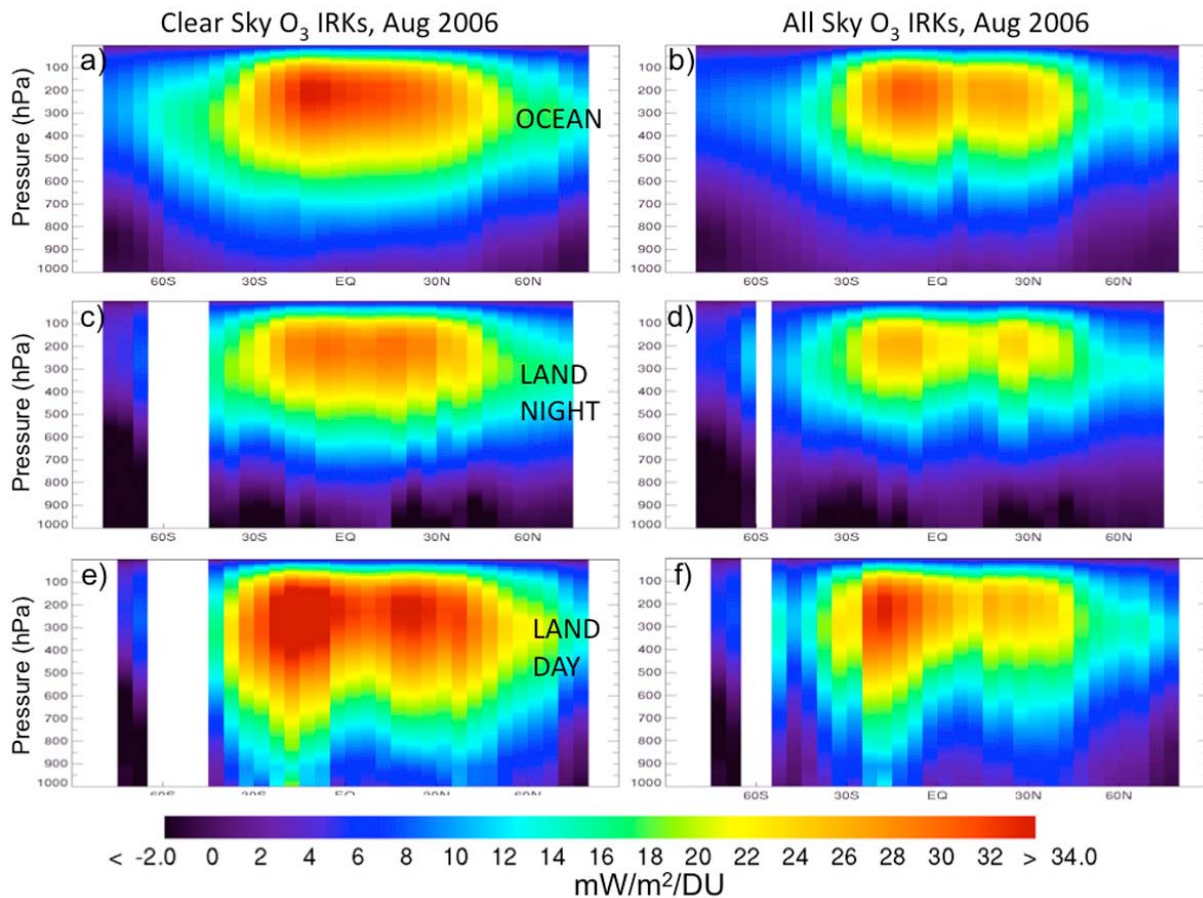


Figure 4. Zonal average IRKs. Same as Figure 3 but with respect to layer column ozone in $\text{mW/m}^2/\text{DU}$.

[32] 2. The previous flux estimates used a fixed value for anisotropy, $R(\theta = 0) = 1.05$ without spectral or scene dependence and produced LWRE values that are too high by about 5% for clear sky ocean scenes. Anisotropy is now estimated as a function of frequency for each observation, with associated random and systematic errors reported.

[33] 3. Results can now be computed for all observations over the full troposphere. We use the thermal tropopause pressure provided from GEOS-4 products by the NASA Goddard Space Flight Center Global Modeling and Assimilation Office (GMAO) [Bloom *et al.*, 2005], interpolated to TES measurement locations.

[34] To date, we have reprocessed August 2006 data only, so we do not have an exact comparison to the annual average reported by Worden *et al.* [2008]. However, we can now show averages, given in Table 3, for both the lower and upper troposphere, over a complete set of observation scenes. These numbers all have a positive sign since LWRE represents a reduction in TOA longwave flux. The value given here for August 2006 upper tropospheric ozone LWRE, 45°S to 45°N for clear sky ocean is consistent with the previously estimated annual average LWRE (within 1σ). Figure 6 shows the global variability in all sky LWRE from TES measurements for tropospheric ozone averaged in $2^\circ \times 2^\circ$ grid boxes. Spatial patterns for the upper tropospheric ozone LWRE over the ocean are similar to the Worden *et al.*

[2008] results. There is a striking difference in magnitudes globally. While the global average is 0.33 W/m^2 , there is a strong zonal dependence on the magnitude with large values across the midlatitudes (up to 1 W/m^2) compensated by very low values in the polar regions. Meridional changes for

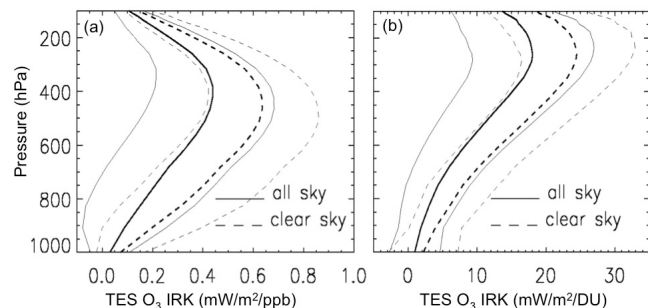


Figure 5. August 2006 global average ozone IRK profiles for all-sky (thick solid line) and clear-sky conditions (thick dashed line). Thin lines indicate $\pm 1\sigma$ standard deviations. (a) The vertical distribution for IRK with respect to ozone changes in mixing ratio (ppb) and (b) the vertical distribution of IRK with respect to column ozone changes in Dobson units (DU).

Table 3. Tropospheric Ozone Longwave Radiative Effect (LWRE) Averages, Uncertainties, Bias, and Standard Deviations (σ) for August 2006

Spatial Regime	Clear-Sky LWRE (W/m^2)	All-Sky LWRE (W/m^2)
Upper troposphere (all lat.)	$0.35 \pm 0.02^{+0.02}_{-0.007}$ ($\sigma = 0.17$)	$0.25 \pm 0.02^{+0.014}_{-0.005}$ ($\sigma = 0.16$)
Lower troposphere (all lat.)	$0.15 \pm 0.01^{+0.01}_{-0.003}$ ($\sigma = 0.09$)	$0.08 \pm 0.01^{+0.004}_{-0.002}$ ($\sigma = 0.08$)
Troposphere (all lat.)	$0.50 \pm 0.02^{+0.03}_{-0.01}$ ($\sigma = 0.24$)	$0.33 \pm 0.02^{+0.018}_{-0.007}$ ($\sigma = 0.23$)
Upper troposphere 45°S–45°N, ocean only	$0.40 \pm 0.02^{+0.022}_{-0.008}$ ($\sigma = 0.13$)	

ocean or land conditions, particularly between Northern Hemisphere Atlantic and Pacific can differ by up to a factor of 2. As expected, maximum values are over land.

[35] In Figure 7, the top panels show zonal average vertical profiles of LWRE (or LIRK) and the standard deviations for clear and all sky cases. The peak in LWRE at around 60–50 hPa is consistent with cooling rate calculations for a standard midlatitude summer atmosphere shown by *Clough and Iacono* [1995]. Figure 7 (middle) shows the standard deviation at each pressure and latitude band with larger variability for the all sky ensembles, which are driven by sensitivity changes induced by cloud variations. For clear sky observations, there is significant variability at 700–800 hPa in the midlatitudes even though the absolute value is relatively low. This variability reflects the mixing of relatively polluted, warm land conditions with clean, cooler oceanic conditions. Figure 7 (bottom) shows zonal average ozone profiles, corrected for the TES tropospheric ozone bias. Although the largest values of LWRE are in the stratosphere, the stratosphere does not contribute as much to the relative variability ($\sigma_{\text{LWRE}}/\text{LWRE}$), which is higher in the troposphere.

[36] As shown in Figures 6 and 7, ozone LWRE is reduced in the tropics, especially in areas associated with higher water vapor abundance such as the warm pool in the western Pacific. This relationship can be quantified for these measurements by correlating clear sky ozone LWRE with precipitable water vapor (prWV) for the tropics (15°S to 15°N) over land and ocean, for day and night as shown in Figure 8. For the slope of ozone LWRE/prWV in $\text{W/m}^2/\text{cm}$ (prWV), we find similar behavior for ocean day and night cases, but very different behavior for ocean compared to land and land day versus land night. The data points are color coded by surface temperature to show the corresponding relationship of prWV with surface temperature, which has the opposite behavior for ocean and land/day cases. Tropospheric ozone LWRE also increases with surface temperature over land for daytime cases due to the larger thermal contrast giving the different dependence of ozone LWRE on prWV for land/day versus land/night and ocean cases.

6. Summary and Conclusions

[37] Using TES Jacobians for the TOA spectral radiance change with respect to the vertical distribution of ozone, computed at the convergence point for ozone retrievals, we have produced instantaneous radiative kernels (IRKs) that represent the sensitivity of the OLR to ozone for all observation scenes including clear, cloudy, ocean and land. This study presented the methods for computing IRKs and initial results from a single month (August 2006). Future work will

show the seasonal dependence and better characterize bias due to TES sampling. From the distributions for August 2006, we find that clouds have a significant effect on the spatial dependence of IRKs and shift the peak sensitivity higher in the troposphere compared to clear sky IRKs. We have also shown the global distribution of LWRE from tropospheric ozone and its dependence on precipitable water in the tropics. We find an all-sky global average TOA longwave radiative effect from tropospheric ozone, (i.e., the reduction in OLR), of $0.33 \pm 0.02^{+0.018}_{-0.007} \text{ W/m}^2$, with significant variability, $\sigma = 0.23 \text{ W/m}^2$.

[38] The next release of TES data products will include the ozone IRKs, which will allow comparisons with model calculations of the same quantity for sensitivity studies of ozone changes in climate models over the 5+ years of TES data. The TES IRKs can also be used independently for assessments of the corresponding change in OLR due to ozone changes resulting from actual or simulated increases or reductions. Since the IRKs will be available with all the TES data products, it will be possible to analyze the dependence of OLR sensitivity to ozone on other conditional variables such as surface emissivity, temperature lapse rate, and cloud parameters. For this study, we have focused on the longwave radiative effect of tropospheric ozone. However, this framework does provide the means to calculate a longwave radiative forcing when variations in ozone can be attributed to anthropogenic sources. Using TES IRKs to

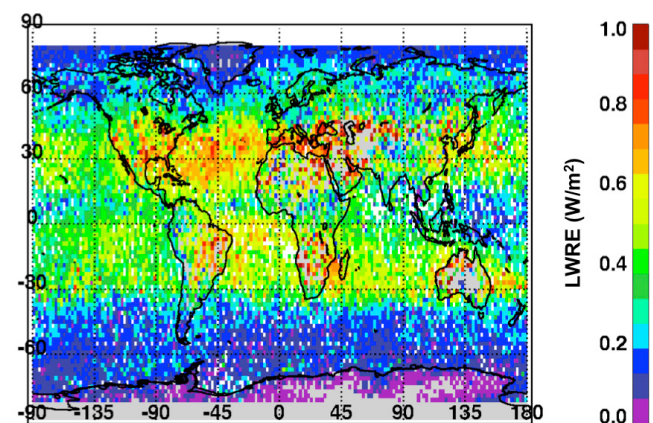


Figure 6. TOA Longwave Radiative Effect (LWRE) in W/m^2 from tropospheric ozone, all-sky conditions, August 2006 TES observations. Data are averaged in $2^\circ \times 2^\circ$ grid cells. Areas with no data are indicated in white over oceans and gray over land. Bins have an average of 3.2 data samples, with a range of 1 to 15 samples per bin.

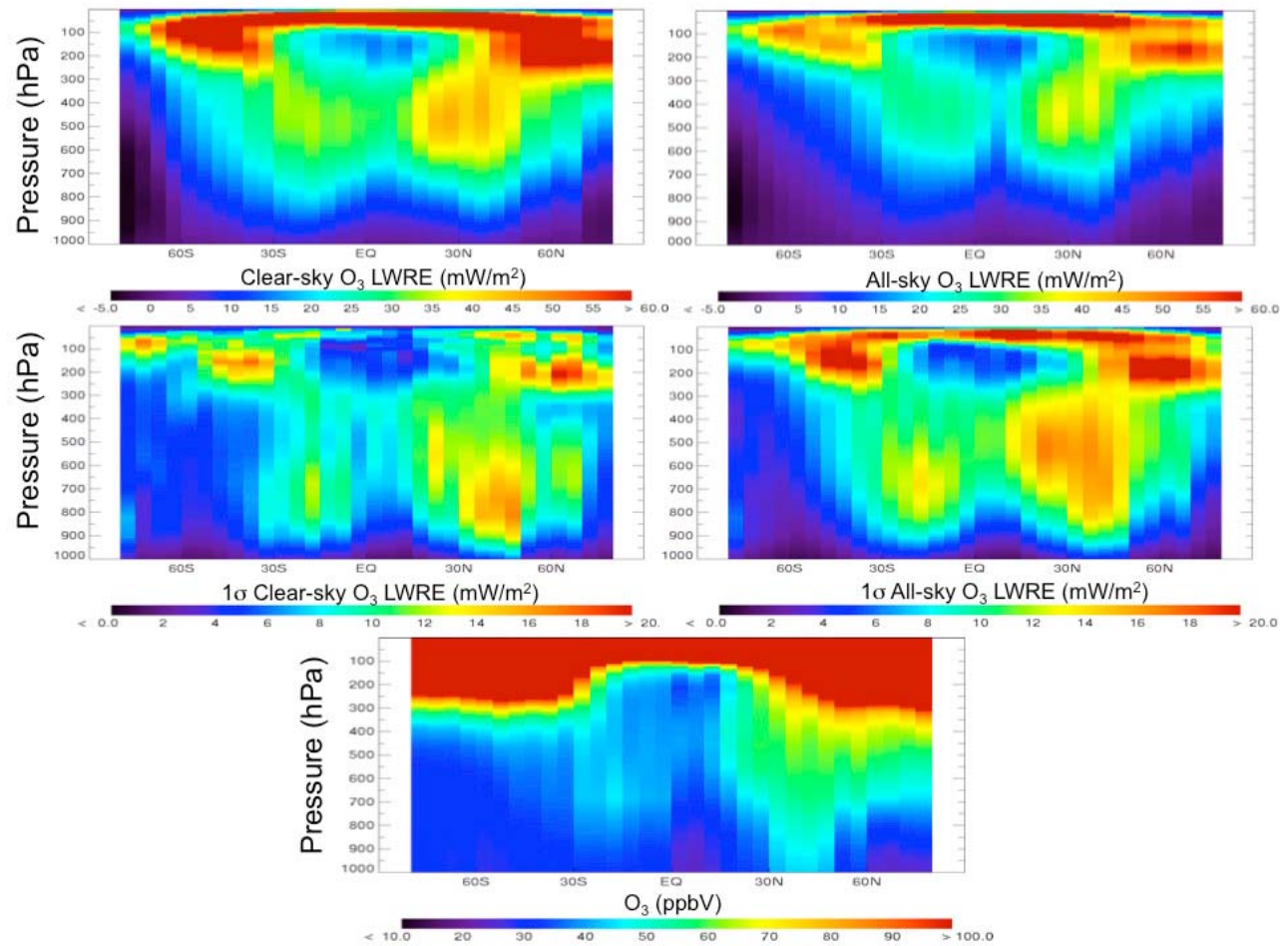


Figure 7. August 2006 zonal average ozone LWRE profiles for clear-sky and all-sky conditions. (top) LWRE and (middle) standard deviation in LWRE. (bottom) The (all-sky) zonal average ozone profiles.

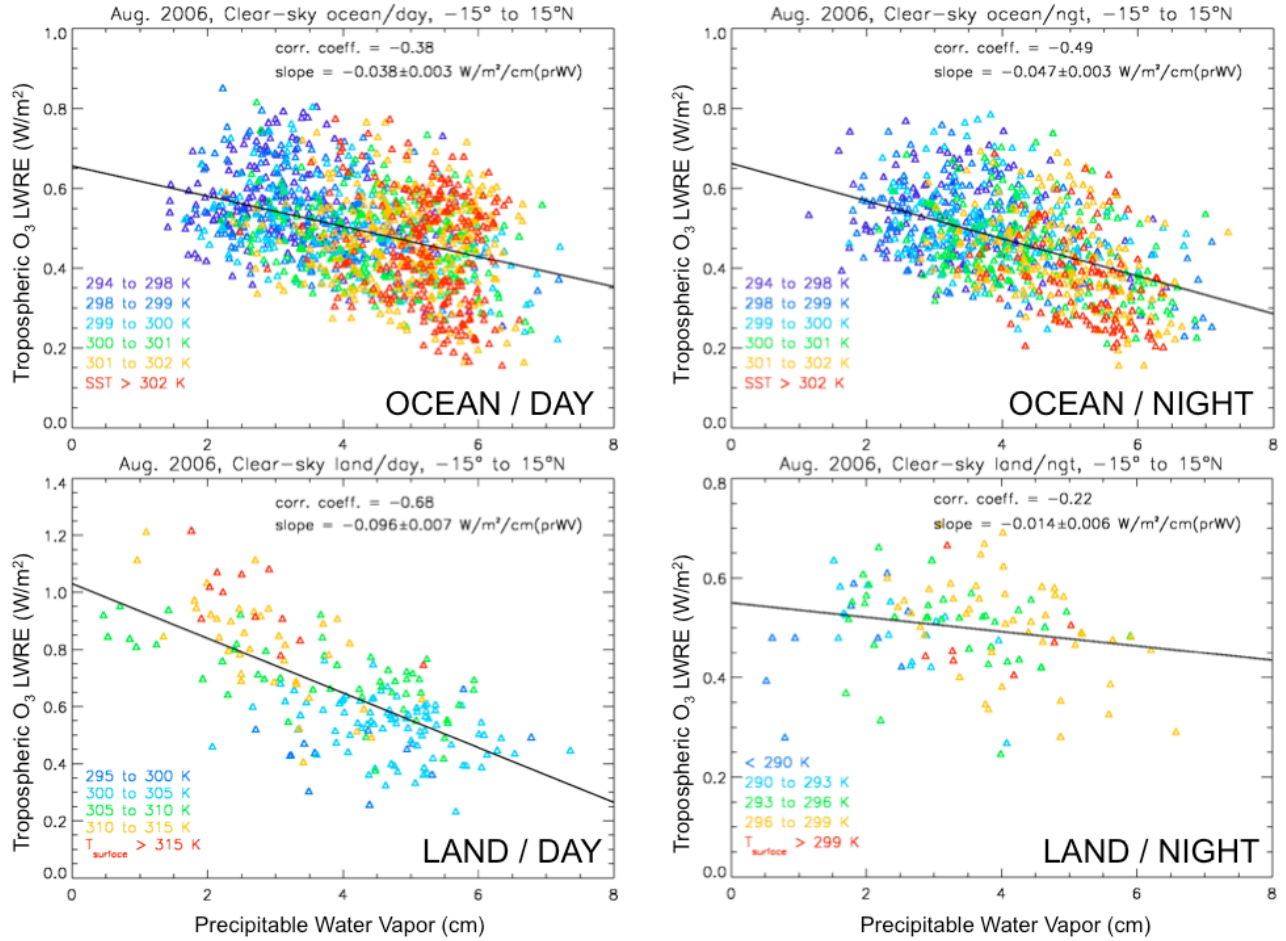


Figure 8. Correlation of tropospheric O₃ LWRE and precipitable water vapor (prWV) for clear-sky tropical conditions (15°S to 15°N). Data points are color coded by the corresponding sea surface temperature (SST) or surface temperature (T_{surface}) range in K (see legends). The black lines show linear fits with corresponding slopes and correlations indicated in each plot.

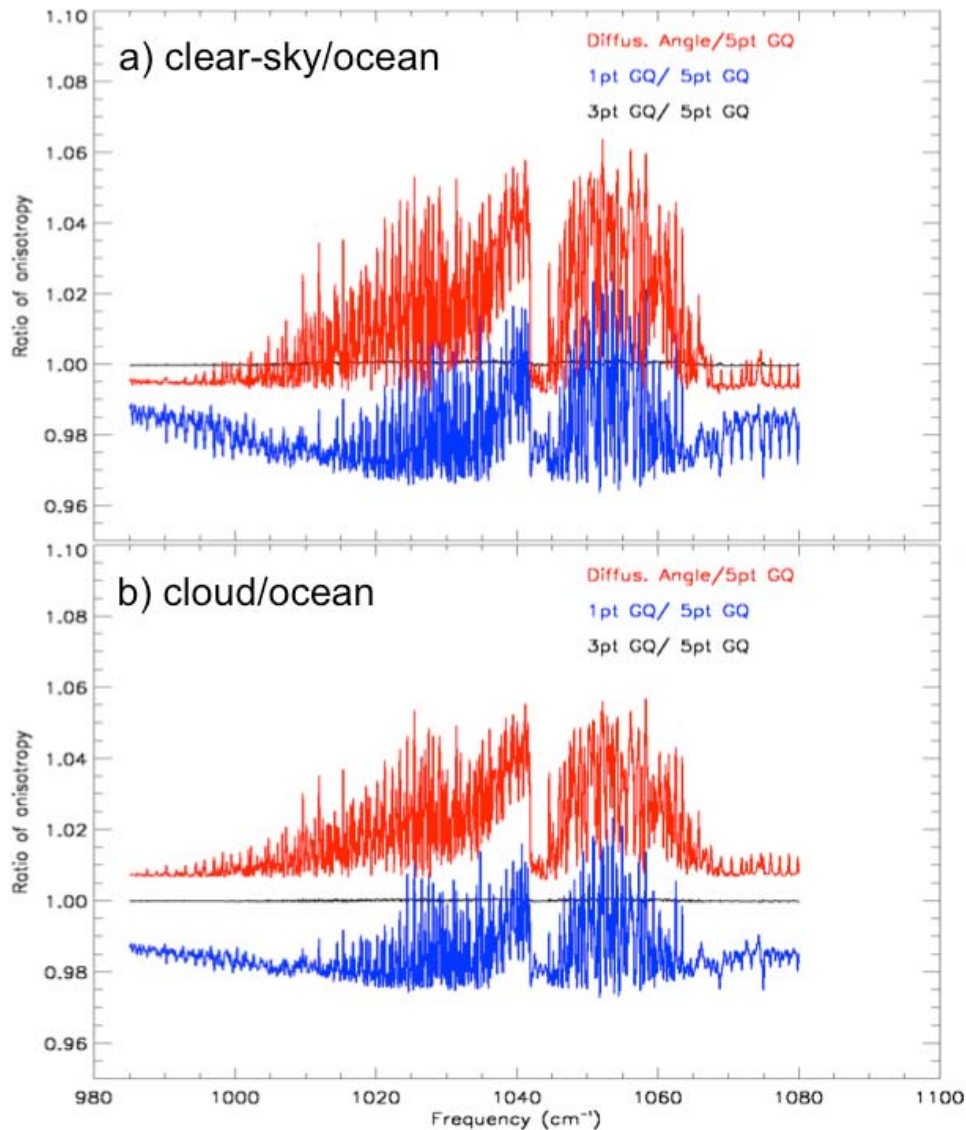


Figure A1. Ratios of anisotropy estimates for single TES ocean scenes with (a) clear sky and (b) cloud at 655 hPa with OD = 0.76.

estimate radiative forcing from anthropogenic ozone is a subject of future research.

Appendix A: TES Anisotropy Estimates

A1. Comparison With Other Methods for Estimating Anisotropy

[39] In order to have a TES anisotropy estimate that can be computed for each TES observation, the algorithm described in section 3.2 is very simplistic, using only one off-zenith angle in the Gaussian Quadrature (GQ) integration. This estimate uses TOA spectral radiances from the TES forward model [Clough *et al.*, 2006] for a nadir view and an off-nadir view at 41.8° (corresponding target zenith angles are 0 and 48°, respectively). In this appendix, we show how this estimate compares to more exact calculations with 3-point and 5-point GQ along with a single ray calculation at the stan-

dard diffusivity angle ($\cos^{-1}(1/1.66)$ or 52.96°). We also show that this estimate demonstrates the expected behavior with respect to scene type, cloud interference and precipitable water vapor as compared to CERES Angular Distribution Model (ADM) values for nadir angles at: <http://asd-www.larc.nasa.gov/Inversion/adm/adm.html>.

[40] Figure A1 shows the ratios of anisotropy estimates for a two TES ocean scenes (clear-sky and cloud) with respect to the anisotropy estimate using 5-point GQ. The 1-point GQ works better at the frequencies with the strongest ozone absorption features while the diffusivity angle would give a better estimate in the more transmissive spectral ranges, as expected [Li, 2000]. Both of the single angle estimates give a 2% integrated bias for clear sky (with opposite sign). The 1-point GQ gives a 1.5% integrated error in the cloud case. Future work will quantify this bias for all scene types,

Table A1. Statistics for TES Anisotropy Estimates, Extrapolated to the CERES Window (WN) Frequency Range for August 2006, 60°S–60°N, Clear-Sky Cases With Average Effective OD < 0.1 as Compared to CERES Values for the Same Scene Types

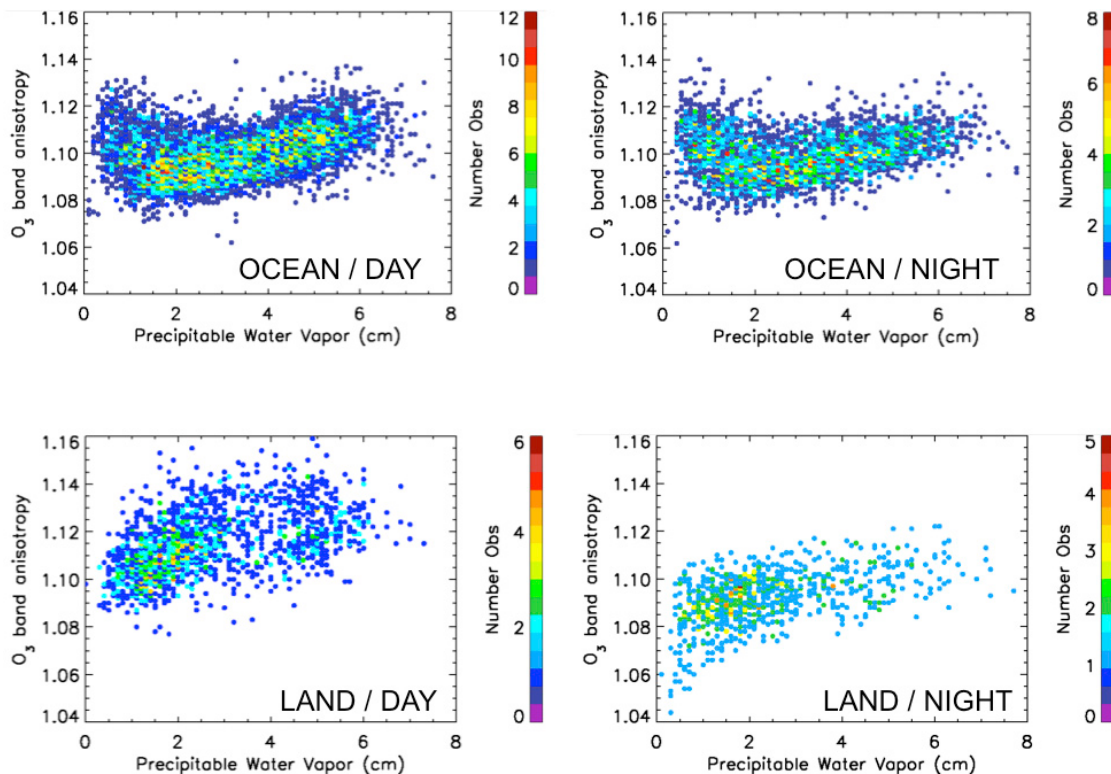
Clear-Sky Observation Type	Precipitable Water Vapor Range (cm)	TES Average Anisotropy for WN Range	TES Standard Deviation Anisotropy	Number of TES Cases	CERES WN Average	CERES WN Standard Deviation
Ocean, night	<2.34	1.046	0.007	1232	1.038	0.009
	2.34 to 3.64	1.047	0.006	737	1.044	0.004
	>3.64	1.055	0.008	1117	1.060	0.002
Ocean, day	<2.29	1.045	0.007	1755	1.038	0.010
	2.29 to 3.48	1.046	0.007	1261	1.044	0.004
	>3.48	1.055	0.009	2419	1.059	0.003
Land, night	<1.56	1.040	0.009	202	1.016	0.022
	1.56 to 2.93	1.043	0.008	228	1.036	0.008
	>2.93	1.049	0.009	191	1.050	0.006
Land, day	<1.43	1.047	0.008	256	1.055	0.030
	1.43 to 2.75	1.055	0.009	462	1.076	0.020
	>2.75	1.069	0.011	476	1.088	0.014

and improve the estimate as needed with higher order GQ if more computing resources are available.

A2. Comparison With CERES Window Range Anisotropy Values

[41] By extrapolating the end values of the TES estimated anisotropy over the 985–1080 cm^{-1} range to the CERES window (WN) band range: 833–1250 cm^{-1} , and integrating over frequency, we can approximate the result for a radiometer and compare this to CERES clear sky ADMs. Comparisons of TES estimates of anisotropy over the window range (WN)

with CERES values at view zenith angle (VZA) in the 0°–10° category are reported in Table A1. CERES values are taken from the tables available at the Website listed above and correspond to the same scene types (clear sky land/ocean, day/night) and precipitable water vapor ranges. The CERES values for clear sky include all seasons, and are also tabulated by the temperature difference from surface to 300 hPa. For the TES cases used here (August, 2006, 60°S to 60°N, ~1:30 local solar time), this temperature difference was always in the highest range for the CERES table parameters. As seen in Table A1, TES and CERES anisotropy values are

**Figure A2.** TES anisotropy estimate summed over the O₃ band (985–1080 cm^{-1}) versus precipitable water vapor for August 2006, 60°S to 60°N, over (top left) ocean clear sky, day, (top right) ocean clear sky, night, (bottom left) land clear sky, day, and (bottom right) land clear sky, night.

reasonably consistent given the different measurement types and extrapolation of the TES spectral anisotropy, and show the same behavior with precipitable water vapor (prWV).

A3. Anisotropy Dependence on Precipitable Water Vapor and Cloud Optical Depth

[42] Figure A2 shows the average anisotropy over the O_3 band (985–1080 cm^{-1}) versus precipitable water vapor in number density plots for clear sky scenes. All scene types show an increase with prWV consistent with Table A1.

[43] Figure A3 shows the behavior of TES ocean anisotropy estimates with effective cloud optical depth (OD). Comparing with CERES ocean ADMs, we see a similar relative behavior with cloud coverage, i.e., increased anisotropy compared to clear sky (region a) for broken clouds with increased cloud coverage (similar to TES transmissive cloud scenes with increased effective OD, region b) and lower anisotropy compared to clear sky for high altitude overcast scenes with high emissivity (similar to TES opaque cloud scenes, region c). The threshold of 0.1 effective OD for clear versus cloudy sky scenes seems appropriate given the uniform character of anisotropy below this.

Appendix B: TES Pressure Levels

[44] The TES pressure grid for forward model radiance and Jacobian calculations, as well as reporting retrieved profiles, is defined on 66 levels using 24 levels per decade from 1000 hPa to 10 hPa and fewer levels per decade from 10 hPa to 0.1 hPa with values shown in Table B1. Although retrieved profiles are reported on this grid, they should not be construed as independent. A posteriori correlations are obtained from the reported error covariance with each retrieval.

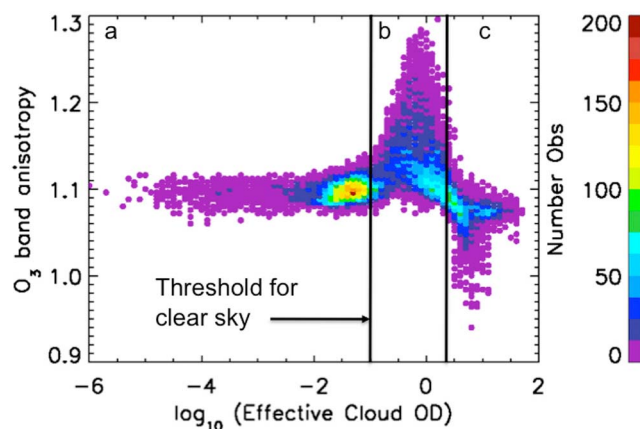


Figure A3. Number density of TES estimated ozone band anisotropy versus retrieved effective cloud optical depth (OD) for August 2006, ocean scenes, 60°S to 60°N. Black lines separate regions corresponding to effective transmission T for: region a: $T > 0.9$; region b: $0.9 > T > 0.1$; and region c: $T < 0.1$. An effective OD of 0.1 or less is the threshold used in this study to identify clear-sky scenes.

Table B1. TES Pressure Levels

TES Level N	Pressures (hPa)					
	N+0	N+1	N+2	N+3	N+4	N+5
1	1211.53	1100.70				
3	1000.00	908.514	825.402	749.893	681.291	618.966
9	562.342	510.898	464.160	421.698	383.117	348.069
15	316.227	287.298	261.016	237.137	215.444	195.735
21	177.829	161.561	146.779	133.352	121.152	110.069
27	100.000	90.852	82.541	74.990	68.130	61.896
33	56.234	51.090	46.416	42.170	38.312	34.807
39	31.623	28.730	26.102	23.714	21.544	19.573
45	17.783	16.156	14.678	13.335	12.115	11.007
51	10.000	9.085	8.254	6.813	5.109	4.642
57	3.162	2.610	2.154	1.616	1.334	1.000
63	0.681	0.383	0.215	0.100		

[45] **Acknowledgments.** This work would not be possible without the contributions of the TES team at the Jet Propulsion Laboratory. We also thank A. Conley and J. F. Lamarque at NCAR as well as Xianglei Huang at University of Michigan for their helpful suggestions. The research described in this paper was funded under a NASA ROSES contract received by K.W.B. and H.M.W. and partially carried out at the Jet Propulsion Laboratory, California Institute of Technology. The National Center for Atmospheric Research (NCAR) is sponsored by the National Science Foundation.

References

- Abramowitz, M., and I. Stegun (1972), *Handbook of Mathematical Functions*, Dover, Mineola, N. Y.
- Aghedo, A. M., K. W. Bowman, H. M. Worden, S. S. Kulawik, D. T. Shindell, J. F. Lamarque, G. Faluvegi, M. Parrington, D. B. A. Jones, and S. Rast (2011), The vertical distribution of ozone instantaneous radiative forcing from satellite and chemistry climate models, *J. Geophys. Res.*, **116**, D01305, doi:10.1029/2010JD014243.
- Beer, R. (2006), TES on the Aura mission: Scientific objectives, measurements, and analysis overview, *IEEE Trans. Geosci. Remote Sens.*, **44**(5), 1102–1105, doi:10.1109/TGRS.2005.863716.
- Bloom, S., et al. (2005), *Documentation and validation of the Goddard Earth Observing System (GEOS) Data Assimilation System—Version 4*, NASA/TM-2005-104606, vol. 26, 165 pp., NASA Goddard Space Flight Cent., Greenbelt, Md.
- Bowman, K., J. Worden, T. Steck, H. Worden, S. Clough, and C. Rodgers (2002), Capturing time and vertical variability of tropospheric ozone: A study using TES nadir retrievals, *J. Geophys. Res.*, **107**(D23), 4723, doi:10.1029/2002JD002150.
- Bowman, K. W., et al. (2006), Tropospheric emission spectrometer: Retrieval method and error analysis, *IEEE Trans. Geosci. Remote Sens.*, **44**(5), 1297–1307, doi:10.1109/TGRS.2006.871234.
- Boynard, A., C. Clerbaux, P.-F. Coheur, D. Hurtmans, S. Turquety, M. George, J. Hadji-Lazaro, C. Keim, and J. Meyer-Arnek (2009), Measurements of total and tropospheric ozone from IASI: Comparison with correlative satellite, ground-based and ozonesonde observations, *Atmos. Chem. Phys.*, **9**, 6255–6271.
- Clough, S. A., and M. J. Iacono (1995), Line-by-line calculation of atmospheric fluxes and cooling rates: 2. Application to carbon dioxide, ozone, methane, nitrous oxide and the halocarbons, *J. Geophys. Res.*, **100**(D8), 16,519–16,535, doi:10.1029/95JD01386.
- Clough, S. A., et al. (2006), Forward model and Jacobians for Tropospheric Emission Spectrometer retrievals, *IEEE Trans. Geosci. Remote Sens.*, **44**(5), 1308, doi:10.1109/TGRS.2005.860986.
- Eldering, A., S. S. Kulawik, J. Worden, K. Bowman, and G. Osterman (2008), Implementation of cloud retrievals for TES atmospheric retrievals: 2. Characterization of cloud top pressure and effective optical depth retrievals, *J. Geophys. Res.*, **113**, D16S37, doi:10.1029/2007JD008858.
- Forster, P. M. D., and K. P. Shine (1997), Radiative forcing and temperature trends from stratospheric ozone changes, *J. Geophys. Res.*, **102**(D9), 10,841–10,855, doi:10.1029/96JD03510.
- Gauss, M., et al. (2003), Radiative forcing in the 21st century due to ozone changes in the troposphere and the lower stratosphere, *J. Geophys. Res.*, **108**(D9), 4292, doi:10.1029/2002JD002624.

- Harries, J. E., H. Brindley, P. J. Sagoo, and R. J. Bantges (2001), Increases in greenhouse forcing inferred from the outgoing longwave radiation spectra of the Earth in 1970 and 1997, *Nature*, **410**, 355, doi:10.1038/35066553.
- Huang, X. L., W. Z. Yang, N. G. Loeb, and V. Ramaswamy (2008), Spectrally resolved fluxes derived from collocated AIRS and CERES measurements and their application in model evaluation: Clear sky over the tropical oceans, *J. Geophys. Res.*, **113**, D09110, doi:10.1029/2007JD009219.
- Huang, X. L., N. G. Loeb, and W. Z. Yang (2010), Spectrally resolved fluxes derived from collocated AIRS and CERES measurements and their application in model evaluation: 2. Cloudy sky and band-by-band cloud radiative forcing over the tropical oceans over the tropical oceans, *J. Geophys. Res.*, **115**, D21101, doi:10.1029/2010JD013932.
- Joiner, J., M. R. Schoeberl, A. P. Vasilkov, L. Oreopoulos, S. Platnick, N. J. Livesey, and P. F. Levelt (2009), Accurate satellite-derived estimates of the tropospheric ozone impact on the global radiation budget, *Atmos. Chem. Phys.*, **9**, 4447–4465, doi:10.5194/acp-9-4447-2009.
- Kulawik, S. S., J. Worden, A. Eldering, K. Bowman, M. Gunson, G. B. Osterman, L. Zhang, S. A. Clough, M. W. Shephard, and R. Beer (2006), Implementation of cloud retrievals for Tropospheric Emission Spectrometer (TES) atmospheric retrievals: 1. Description and characterization of errors on trace gas retrievals, *J. Geophys. Res.*, **111**, D24204, doi:10.1029/2005JD006733.
- Lacis, A. D., J. Wuebbles, and J. A. Logan (1990), Radiative forcing of climate by changes in the vertical distribution of ozone, *J. Geophys. Res.*, **95**(D7), 9971–9981, doi:10.1029/JD095iD07p09971.
- Levy, H., II, D. Shindell, A. Gilliland, M. Schwarzkopf, and L. W. Horowitz (2008a), CCSP 2008: Climate projections based on emissions scenarios for long-lived and short-lived radiatively active gases and aerosols, report, 100 pp., Natl. Clim. Data Cent., NOAA, Boulder, Colo.
- Levy, H., II, M. D. Schwarzkopf, L. Horowitz, V. Ramaswamy, and K. L. Findell (2008b), Strong sensitivity of late 21st century climate to projected changes in short-lived air pollutants, *J. Geophys. Res.*, **113**, D06102, doi:10.1029/2007JD009176.
- Li, J. (2000), Gaussian quadrature and its application to infrared radiation, *J. Atmos. Sci.*, **57**(5), 753–765, doi:10.1175/1520-0469(2000)057<0753:GQAIAT>2.0.CO;2.
- Loeb, N. G., N. M. Smith, S. Kato, W. F. Miller, S. K. Gupta, P. Minnis, and B. A. Wielicki (2003), Angular distribution models for top-of-atmosphere radiative flux estimation from the Clouds and the Earth's Radiant Energy System instrument on the Tropical Rainfall Measuring Mission Satellite. Part I: Methodology, *J. Appl. Meteorol.*, **42**, 240–265, doi:10.1175/1520-0450(2003)042<0240:ADMFTO>2.0.CO;2.
- Nassar, R., et al. (2008), Validation of Tropospheric Emission Spectrometer (TES) nadir ozone profiles using ozonesonde measurements, *J. Geophys. Res.*, **113**, D15S17, doi:10.1029/2007JD008819.
- Osterman, G., et al. (2008), Validation of Tropospheric Emission Spectrometer (TES) measurements of the total, stratospheric and tropospheric column abundance of ozone, *J. Geophys. Res.*, **113**, D15S16, doi:10.1029/2007JD008801.
- Osterman, G., et al. (Eds.) (2009), TES level 2 data user's guide, v4.0, *JPL D-38042*, JPL, Pasadena, Calif. [Available at <http://tes.jpl.nasa.gov/documents/>]
- Picquet-Varraut, B., J. Orphal, J.-F. Doussin, P. Carlier, and J.-M. Flaud (2004), Laboratory intercomparison of the ozone absorption coefficients in the mid-infrared (10 μm) and ultraviolet (300–350 nm) spectral regions, *J. Phys. Chem. A*, **109**(6), 1008–1014.
- Ramanathan, V., and Y. Xu (2010), The Copenhagen Accord for limiting global warming: Criteria, constraints, and available avenues, *Proc. Natl. Acad. Sci. U. S. A.*, **107**(18), 8055–8062, doi:10.1073/pnas.1002293107.
- Ramaswamy, V., O. Boucher, J. Haigh, D. Hauglustaine, J. Haywood, G. Myhre, T. Nakajima, G. Y. Shi, and S. Solomon (2001), Radiative forcing of climate change, in *Climate Change 2001: The Scientific Basis. Contribution of Working Group I to the Third Assessment Report of the Intergovernmental Panel on Climate Change (IPCC)*, edited by J. T. Houghton et al., pp. 349–416, Cambridge Univ. Press, New York.
- Richards, N. A. D., G. B. Osterman, E. V. Browell, J. W. Hair, M. Avery, and Q. Li (2008), Validation of Tropospheric Emission Spectrometer ozone profiles with aircraft observations during the Intercontinental Chemical Transport Experiment–B, *J. Geophys. Res.*, **113**, D16S29, doi:10.1029/2007JD008815.
- Rothman, L. S., et al. (1987), The HITRAN database: 1986 edition, *Appl. Opt.*, **26**, 4058–4097, doi:10.1364/AO.26.004058.
- Santer, B. D., et al. (2003), Contributions of anthropogenic and natural forcing to recent tropopause height changes, *Science*, **301**(5632), 479–483, doi:10.1126/science.1084123.
- Schneider, M., A. Redondas, F. Hase, C. Guirado, T. Blumenstock, and E. Cuevas (2008), Comparison of ground-based Brewer and FTIR total column O₃ monitoring techniques, *Atmos. Chem. Phys.*, **8**, 5535–5550.
- Seidel, D. J., and W. J. Randel (2007), Recent widening of the tropical belt: Evidence from tropopause observations, *J. Geophys. Res.*, **112**, D20113, doi:10.1029/2007JD008861.
- Shephard, M. W., et al. (2008), Tropospheric Emission Spectrometer nadir spectral radiance comparisons, *J. Geophys. Res.*, **113**, D15S05, doi:10.1029/2007JD008856.
- Shindell, D., and G. Faluvegi (2009), Climate response to regional radiative forcing during the twentieth century, *Nat. Geosci.*, **2**(4), 294–300.
- Sitch, S., P. M. Cox, W. J. Collins, and C. Huntingford (2007), Indirect radiative forcing of climate change through ozone effects on the land-carbon sink, *Nature*, **448**, 791–794.
- Soden, B. J., I. M. Held, R. Colman, K. M. Shell, J. T. Kiehl, and C. A. Shields (2008), Quantifying climate feedbacks using radiative kernels, *J. Clim.*, **21**(14), 3504–3520, doi:10.1175/2007JCLI2110.1.
- Solomon, S., et al. (2007), Technical summary, in *Climate Change 2007: The Physical Science Basis. Contribution of Working Group I to the Fourth Assessment Report of the Intergovernmental Panel on Climate Change, chapter Technical Summary*, edited by S. Solomon et al., pp. 20–90, Cambridge Univ. Press, New York.
- Stevenson, D. S., et al. (2006), Multimodel ensemble simulations of present-day and near-future tropospheric ozone, *J. Geophys. Res.*, **111**, D08301, doi:10.1029/2005JD006338.
- Tobin, D. C., et al. (2006), Radiometric and spectral validation of atmospheric infrared sounder observations with the aircraft-based scanning high-resolution interferometer sounder, *J. Geophys. Res.*, **111**, D09S02, doi:10.1029/2005JD006094.
- van Vuuren, D. P., J. Weyant, and F. de la Chesnaye (2006), Multi-gas scenarios to stabilize radiative forcing, *Energy Econ.*, **28**, 102–120, doi:10.1016/j.eneco.2005.10.003.
- Wallack, S., and V. Ramanathan (2009), The other climate changers: why black carbon and ozone matter, *Foreign Affairs*, **88**, 105–113.
- West, J. J., A. M. Fiore, L. W. Horowitz, and D. L. Mauzerall (2006), Global health benefits of mitigating ozone pollution with methane emission controls, *Proc. Natl. Acad. Sci. U. S. A.*, **103**(11), 3988–3993, doi:10.1073/pnas.0600201103.
- West, J. J., A. M. Fiore, V. Naik, L. W. Horowitz, M. D. Schwarzkopf, and D. L. Mauzerall (2007), Ozone air quality and radiative forcing consequences of changes in ozone precursor emissions, *Geophys. Res. Lett.*, **34**, L06806, doi:10.1029/2006GL029173.
- Worden, H. M., et al. (2006), TES level 1 algorithms: Interferogram processing, geolocation, radiometric, and spectral calibration, *IEEE Trans. Geosci. Remote Sens.*, **44**(5), 1288–1296, doi:10.1109/TGRS.2005.863717.
- Worden, H. M., K. W. Bowman, J. R. Worden, A. Eldering, and R. Beer (2008), Satellite measurements of the clear-sky greenhouse effect from tropospheric ozone, *Nat. Geosci.*, **1**, 305–308, doi:10.1038/ngeo182.
- Worden, J., S. S. Kulawik, M. W. Shephard, S. A. Clough, H. Worden, K. Bowman, and A. Goldman (2004), Predicted errors of tropospheric emission spectrometer nadir retrievals from spectral window selection, *J. Geophys. Res.*, **109**, D09308, doi:10.1029/2004JD004522.

A. M. Aghedo, K. W. Bowman, and S. S. Kulawik, Jet Propulsion Laboratory, California Institute of Technology, 4800 Oak Grove Dr., MS 183-601, Pasadena, CA 91109, USA.

H. M. Worden, Atmospheric Chemistry Division, National Center for Atmospheric Research, Boulder, 3450 Mitchell Ln., Boulder, CO 80301, USA. (hmw@ucar.edu)